

Artificial photosynthesis platform of 2D/2D MXene/crystalline covalent organic frameworks heterostructure for efficient photoenzymatic CO₂ reduction

Jiafu Qu ^{a,1}, Tingyu Yang ^{a,1}, Pengye Zhang ^a, Fengyi Yang ^a, Yahui Cai ^b, Xiaogang Yang ^a, Chang Ming Li ^a, Jundie Hu ^{a,*}

^a School of Materials Science and Engineering, Suzhou University of Science and Technology, Suzhou 215009, China

^b College of Materials Science and Engineering, Nanjing Forestry University, Nanjing 210037, China



ARTICLE INFO

Keywords:

Artificial photosynthesis
Covalent organic frameworks
CO₂ reduction
photoenzymatic catalysis
NADH regeneration

ABSTRACT

Photoenzymatic catalysis is an efficient strategy for selectively converting CO₂ into valuable chemicals. However, the sluggish reaction kinetics, resulting from low visible light utilization and rapid recombination of photo-generated carriers, severely inhibit the yields of target products. Herein, we present a novel artificial photosynthesis platform of 2D/2D MXene/crystalline COF-367 heterostructure for efficient conversion of CO₂ into HCOOH. This platform is extremely sensitive to solar light ($\lambda \leq 750$ nm), with rapid charge separation and transfer due to the well-designed abundant ultrathin 2D/2D hetero-interfaces. Remarkably, Ti₃C₂/COF-367 achieves an impressive yield of 83.38% for coenzyme NADH regeneration with absence of electron mediator. Furthermore, it demonstrates a cascade ultra-high production rate of HCOOH at 1.88 mmol g⁻¹ h⁻¹ with almost 100 % selectivity. This work represents the first example of MXene to promote charge transfer in COFs-based photoenzymatic synergistic catalytic system, and provides insights into the development of organic/inorganic hybrids for CO₂ photoreduction.

1. Introduction

Achieving carbon neutrality is a pressing global challenge [1,2]. Harnessing renewable solar energy to convert carbon dioxide (CO₂) into high-value chemicals offers a green and environmentally friendly solution [3,4]. However, photocatalytic CO₂ reduction faces obstacles in terms of catalytic activity and product selectivity, primarily due to competing multi-electron reduction processes and H₂-evolution reactions [5,6]. Therefore, drawing inspiration from natural plant photosynthesis, photoenzymatic synergistic catalysis may prove effective in addressing these challenges by skillfully combining enzyme chemical-specificity and high activity [7].

In the photoenzymatic catalytic process, cofactor nicotinamide adenine dinucleotide (NADH) plays a crucial role in activating reductases such as formate dehydrogenase (FDH), peroxidases, and alcohol dehydrogenases [8,9]. Nevertheless, the high cost [10], instability and large demand of NADH pose significant challenges for practical application in industries [11]. To address this, *in situ* NADH

regeneration is urgently needed for photoenzymatic cascade catalytic systems. Previous studies have utilized electron mediator, such as [Cp^{*}Rh(bpy)H]⁺ [12] and [Cp^{*}RhCl₂]₂ [9] to achieve efficient NADH regeneration and CO₂ reduction. However, these approaches rely on expensive noble metal Rh-based complexes, increasing the overall cost [13]. Therefore, developing an *in situ* photocatalytic NADH regeneration system and cascade CO₂ reduction without electron mediator would be highly valuable.

Conjugated organic frameworks (COFs) show great promise in photocatalytic CO₂ reduction [14], especially in photoenzymatic catalysis due to their excellent biocompatibility, which is only in its infancy and urgently needs to be explored in depth. They offer unique advantages including highly ordered stacking sequences, strong π - π electron delocalization, large specific surface area and inherent porosity [15,16]. The tunable nature of COFs allows for the precise customization of structures, regulating visible light response and local electron density to improve the catalytic activity [17]. Imine-linked COFs, in particular, are attractive due to the high bond energy and dynamic reversibility of

* Corresponding author.

E-mail address: hjd@usts.edu.cn (J. Hu).

¹ These authors contributed equally to this work.

imine bonds, resulting in stable structures and facilitate rapid charge transfer [18]. Porphyrin and its derivatives are ideal precursor molecular units for COFs, with their tetrapyrrole structure, unique conjugated π -electron macrocyclic ring system, and stacked 2D layered structure with overlapped conjugation of π -orbitals [19]. These characteristics enable the formation of π -electron channels within the deep stacking holes and interlayer, facilitating the smooth transportation of photo-generated charges under visible light irradiation [20]. However, excessive charge accumulation on COFs units can lead to recombination

and loss of catalytic activity. Therefore, the introduction of electron acceptors to construct abundant hetero-interfaces can effectively transfer the accumulated electrons on COFs, thereby enhancing the photocatalytic CO_2 conversion performance [21]. Transition metal-based materials have been certified to be the effective materials for facilitating electron transport [22,23]. MXene, an emerging 2D layered transition metal material ($\text{Ti}_3\text{C}_2\text{T}_x$), is an excellent electron acceptor due to its high conductivity, abundant active sites and charge mobility anisotropy [24]. Moreover, MXene demonstrates remarkable sunlight

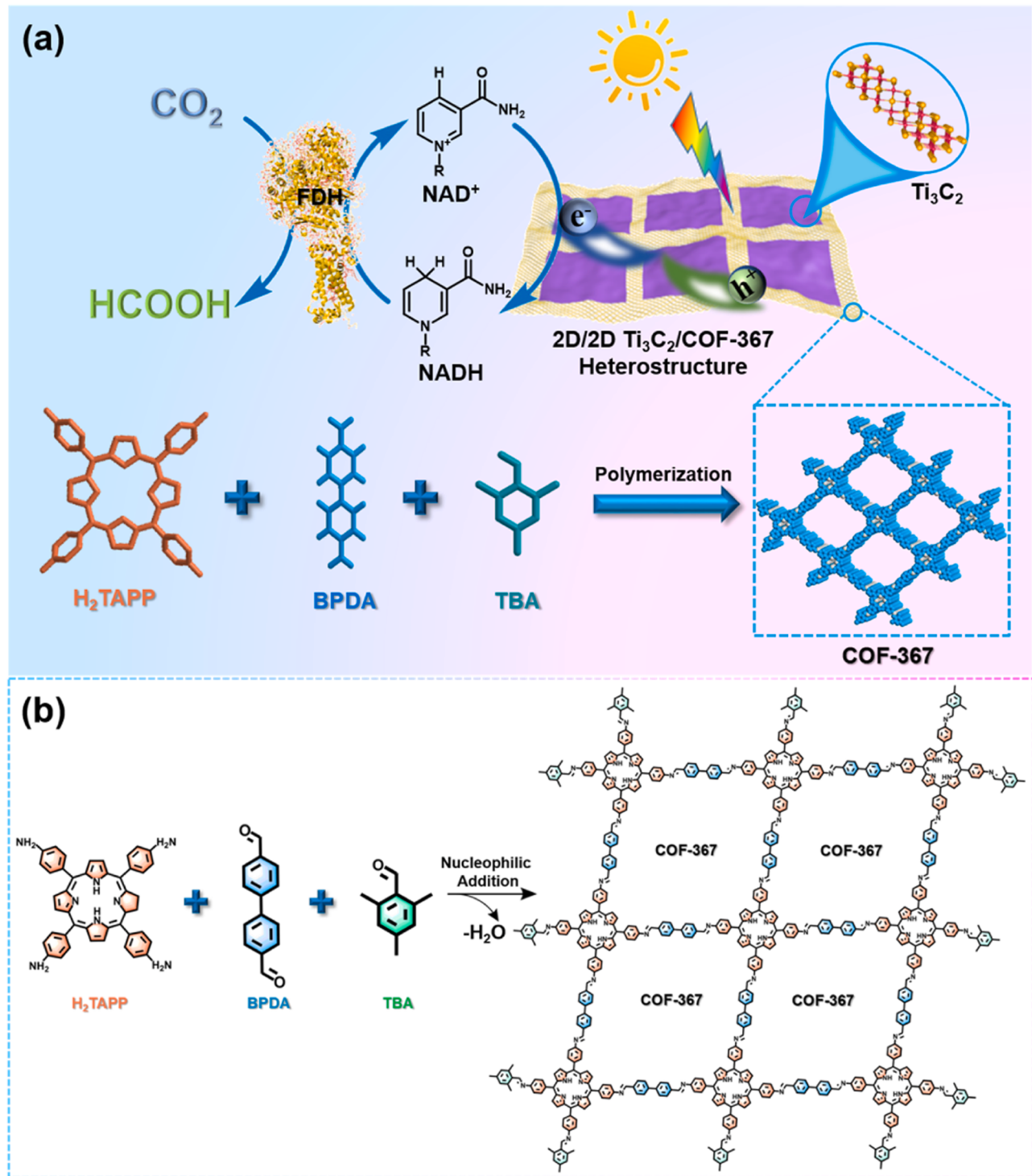


Fig. 1. Schematic presentation of the (a) synthesis and (b) structure of $\text{Ti}_3\text{C}_2/\text{COF-367}$ heterostructure for NADH regeneration and photoenzymatic synergistic catalysis of CO_2 to HCOOH .

absorption properties, enabling it to absorb light energy across the visible and near-infrared spectral range. Consequently, it can be chosen as an ideal candidate for constructing a 2D/2D heterostructure with porphyrin-based imine-linked COFs to enhance the utilization of photogenerated carriers and facilitate CO₂ conversion.

Herein, we present a novel 2D/2D MXene/crystalline imine-linked COFs heterostructure for efficient NADH regeneration and photoenzymatic synergistic cascade catalysis of CO₂ conversion to formic acid (HCOOH) (Fig. 1). The crystalline imine-linked COF-367 is synthesized from the monomers 5,10,15,20-tetrakis(4-aminophenyl)-21H,23H-porphine (H₂TAPP) and 4,4-biphenyldicarboxaldehyde (BPDA). According to the geometric shapes, H₂TAPP is the molecule with a quadratic axis of symmetry (C₂), while BPDA is the molecule with four axes of symmetry (C₄) [25,26]. Thus, the imine-linked COF-367 exhibits a “C₂+C₄” symmetry combination with controlled growth along the planar directions using (TBA). Ti₃C₂ is employed as an electron acceptor to enhance charge transfer, visible light response, and expose more active sites. The well-designed 2D/2D Ti₃C₂/COF-367 heterojunction with abundant interfaces and rapid charge transfer achieves a high NADH yield of 83.38 % without electron mediator or photosensitizer, and an ultra-high HCOOH production rate of 1.88 mmol g⁻¹ h⁻¹ with nearly 100 % selectivity. This study provides valuable insight into the design of molecularly editable COFs-based heterostructure for photoenzymatic catalytic systems.

2. Experimental section

2.1. Photocatalyst preparation

The 2D COF-367 nanosheets were synthesized by solvothermal method [27]. Ti₃C₂ nanosheets were prepared by etching of Ti₃AlC₂ using HF [28]. The Ti₃C₂/COF-367 hybrids were synthesized *via* an in situ growth method [29]. The corresponding products were designated as 5 %, 10 %, 15 % and 20 % Ti₃C₂/COF-367 hybrids, respectively. The detailed prepare procedures were displayed in [Supporting Information](#).

2.2. Characterization

Transmission electron microscopy (TEM) and high-resolution TEM (HRTEM, Hitachi H600 with 200 kV acceleration voltage) equipped with energy dispersive X-ray (EDX) elemental analysis and atomic force microscope (AFM, Bruker Dimension Icon) were performed to investigate the morphology of the photocatalysts. Brunner-Emmett-Teller (BET) test was carried out using a Quantachrome, FL 33426. X-ray diffraction (XRD) was detected on a Bruker D8 Advance (Germany) diffractometer with Cu K α radiation. Fourier-transform infrared (FT-IR) spectra were recorded using a Nicolet Is50 FT-IR spectrometer. Solid-state ¹³C nuclear magnetic resonance (NMR) spectra spectrometry was performed on a Bruker AVANCEIII/WB-400 spectrometer. MALDI-TOF mass spectrometry (MALDI-MS) was detected on Bruker Ultraflextreme with 355 nm Nd:YAG laser. UV-Vis diffuse reflectance spectra (DRS) were obtained using a Shimadzu UV-3600 DRS with integrating sphere. Shimadzu and RF-6000 Edinburgh FL/FSTCSPC920 monitored steady-state photoluminescence (PL) spectra and time-resolved photoluminescence (TRPL), respectively. X-ray photoelectron spectroscopy (XPS) was examined on ESCALAB 250Xi spectrometer. The electron spin resonance (ESR) g-factor was recorded on the Bruker Desktop microESR. Transient surface photovoltage (TSPV) tests were performed with 355 nm laser pulse (Nd:YAG laser, Q-smart 450, Quantel). Electrochemical properties of samples were measured on CHI 660E electrochemical system (Chenhua, Shanghai) with a standard three-electrode cell, where Ag/AgCl, Pt sheet and samples/ITO were used as the reference electrode, counter electrode, and working electrode, respectively. In these tests, Na₂SO₄ (0.1 M), KCl (0.5 M) solution of K₃[Fe(CN)₆]/K₄[Fe(CN)₆] (5.0 mM) were applied as electrolytes to examined transient photocurrent response and electrochemical impedance

spectroscopy (EIS), respectively. Moreover, Na₂SO₄ (0.2 M) was used as electrolyte for Mott-Schottky (M-S) plots at three different frequencies (0.5, 1.0 and 1.5 kHz).

2.3. Photocatalytic evaluation

Photocatalytic NADH regeneration: The photocatalytic NADH regeneration experiments were carried out using a multichannel photocatalytic reaction system (PerfectLight PCX-50 C DISCOVER, 9 sites) equipped with a simulated sunlight source (AM 1.5, 100 mW cm⁻²). In each quartz reactor, 10 mg of catalysts, β -NAD⁺ (1 mM), TEOA (15 wt %), and a phosphate buffer solution (10 mL, 100 mM, pH = 8) were added and sonicated to ensure uniform dispersion. The photocatalytic reaction was initiated at room temperature (25 °C) after a 0.5 h adsorption-desorption equilibrium dark treatment [17]. The concentration of produced NADH were measured hourly by the peak intensity at 340 nm using a spectrophotometer (UV-3600, Shimadzu).

Photoenzymatic CO₂ reduction: The experiment of photoenzymatic CO₂ reduction to HCOOH was also performed in the aforementioned multichannel system. Generally, 10 mL of phosphate buffer solution (pH = 7.4, 100 mM) containing β -NAD⁺ (0.1 mM), TEOA (15 wt%), FDH (3 U) and 10 mg of catalysts were mixed into quartz reactors with lids, the containing NaHCO₃ (50 mM) was used as the only carbon source of CO₂ [30]. Similar to the NADH regeneration experiment, the photoenzymatic CO₂ reduction reaction was started after the adsorption-desorption equilibrium process. The gas products were detected by gas chromatography (Agilent 7890B), and the yields of liquid products were measured by anion exchange chromatography (CIC-D100, Shenghan) every 0.5 h.

2.4. Computational details

All calculations are performed within the framework of density functional theory (DFT) with the projector augmented plane-wave method, as implemented in the Vienna ab initio simulation package (VASP) [31]. The exchange-correlation potential is described by the Perdew-Burke-Ernzerhof (PBE) generalized gradient approximation [32]. A plane wave cut-off energy of 520 eV is used, and the energy criterion for the iterative solution of the Kohn-Sham equation is set to 10⁻⁶ eV. The atomic structures are relaxed until the residual forces on the atoms are less than 0.02 eV/Å.

3. Results and discussion

The 2D/2D MXene/crystalline imine-linked COFs heterostructures were fabricated using an in situ growth method, in which Ti₃C₂ nanosheets were obtained through HF-etching, while imine-linked COF-367 was synthesized *via* solvothermal nucleophilic addition reaction (Fig. 1b, Fig. S1). To achieve ultrathin 2D nanosheets of COF-367, rigid TBA molecules were introduced at their edges through imine exchange, taking advantage of the dynamic reversibility nature of imine bond [33]. This approach not only prevents their axial π - π stacking into bulk structures but also promotes their anisotropic growth along the planar direction. Similarly, 2D/2D Ti₃C₂/COF-367 hybrids with abundant hetero-interfaces were constructed by in situ growth of ultrathin COF-367 on the MXene surface, which provide a rich channel for the rapid transfer of photogenerated carriers.

3.1. Microstructure characterization

The microstructures of synthesized photocatalysts were characterized using scanning electron microscopy (SEM), TEM, HRTEM, EDX and AFM analysis. Fig. 2a-c illustrates the successful synthesis of highly crystalline imine-linked COF-367 nanosheets with an ultrathin wrinkled morphology, indicating a distinctive 2D structure. The high crystallinity of COF-367 is evident from the clear lattice fringe observed in the

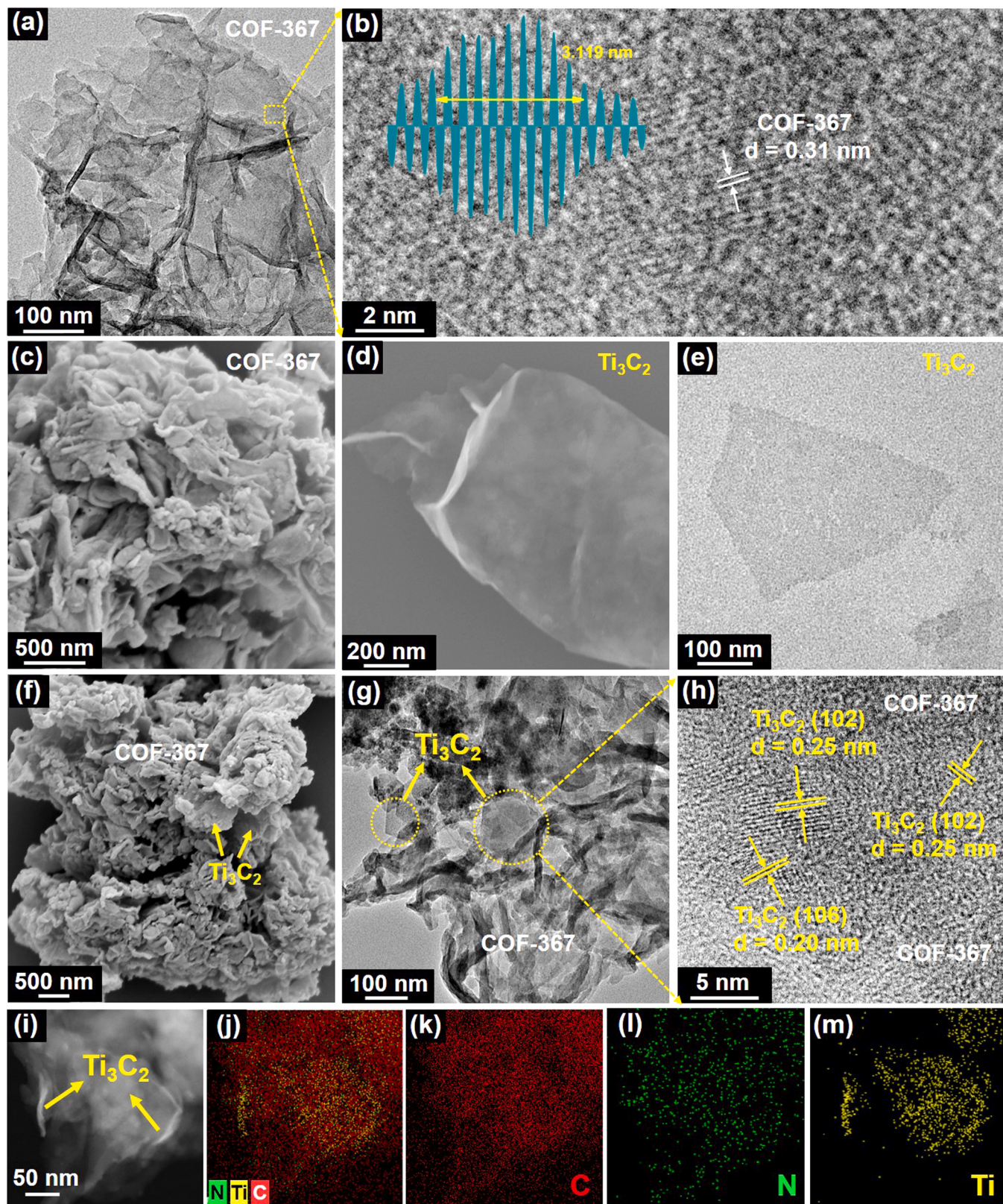


Fig. 2. (a) TEM, (b) HRTEM and (c) SEM images of COF-367 nanosheets. (d) SEM and (e) TEM images of Ti_3C_2 nanosheets. (f) SEM, (g) TEM, (h) HRTEM and (i) STEM images of 2D/2D 10 % Ti_3C_2 /COF-367 heterojunction, corresponding EDX mapping images of (j) layered image, (k) C, (l) N and (m) Ti elements.

HRTEM image, with a stripe spacing of 0.31 nm corresponding to its (220) crystal plane [34]. Simultaneously, exfoliated ultrathin Ti_3C_2 nanosheets were obtained by etching the Al layer of the MXene material. These Ti_3C_2 nanosheets possess a flat and smooth surface with distinct

sharp edges and corners (Fig. 2d-e), making them easily distinguishable from COF-367. The tight stacking of COF-367 on Ti_3C_2 can be observed in Fig. 2f-h, and the 2D/2D hetero-interface of Ti_3C_2 /COF-367 is clearly visible in the enlarged image (Fig. 2h). The lattice-stripe spacing of 0.25

and 0.20 nm in Ti_3C_2 belongs to its (102) and (106) crystal faces, respectively. Notably, the heterostructure of 2D/2D $\text{Ti}_3\text{C}_2/\text{COF-367}$ can be more readily identified through STEM and EDX elemental mapping images (Fig. 2i-m, Fig. S2 and Table S1). The presence of C, N and Ti elements was detected, and the accurate elemental distributions of Ti and N clearly depict the regions of MXene and COF-367, respectively. The trace Cu element in TEM EDX (Fig. S2) comes from the Cu mesh used for supporting samples. These results further confirm the successful construction of the $\text{Ti}_3\text{C}_2/\text{COF-367}$ heterostructure without any other impurities [35]. Moreover, the thickness of COF-367 is probed to be approximately 2.7 nm (Fig. S3), illustrating its thin nanosheet structure.

To investigate the influence of MXene on the active sites of COF materials, we conducted BET tests to determine the specific surface area and pore size distribution of COF-367 and 10 % $\text{Ti}_3\text{C}_2/\text{COF-367}$. The N_2 adsorption-desorption isotherms (Fig. S4) revealed that their specific surface areas were measured to be 79.110 and $82.581 \text{ m}^2 \text{ g}^{-1}$,

respectively, with corresponding pore sizes of 8.78 and 8.91 nm. These similar results indicate that MXene does not significantly affect the catalytic active sites of COF-367. The effect of the smaller or larger pore size have been explored. The smaller pores would inhibit the transfer and contact of molecules, while the larger pores would leaky enzymes [36]. Moreover, the larger pores also reduce the interlayer interaction of COFs and cause structure collapse [37]. As the results, the appropriate pore size of prepared samples can facilitate the transfer of molecules including CO_2 , NADH and FDH during the photoenzymatic reaction, potentially enhancing the reaction rate [38].

3.2. Chemical state and crystal phase

The crystal phase structure of the samples was further characterized using XRD analysis. As depicted in Fig. 3a, the characteristic peaks of Ti_3C_2 at 6.8° and 60.7° can be attributed to its (002) and (110) crystal

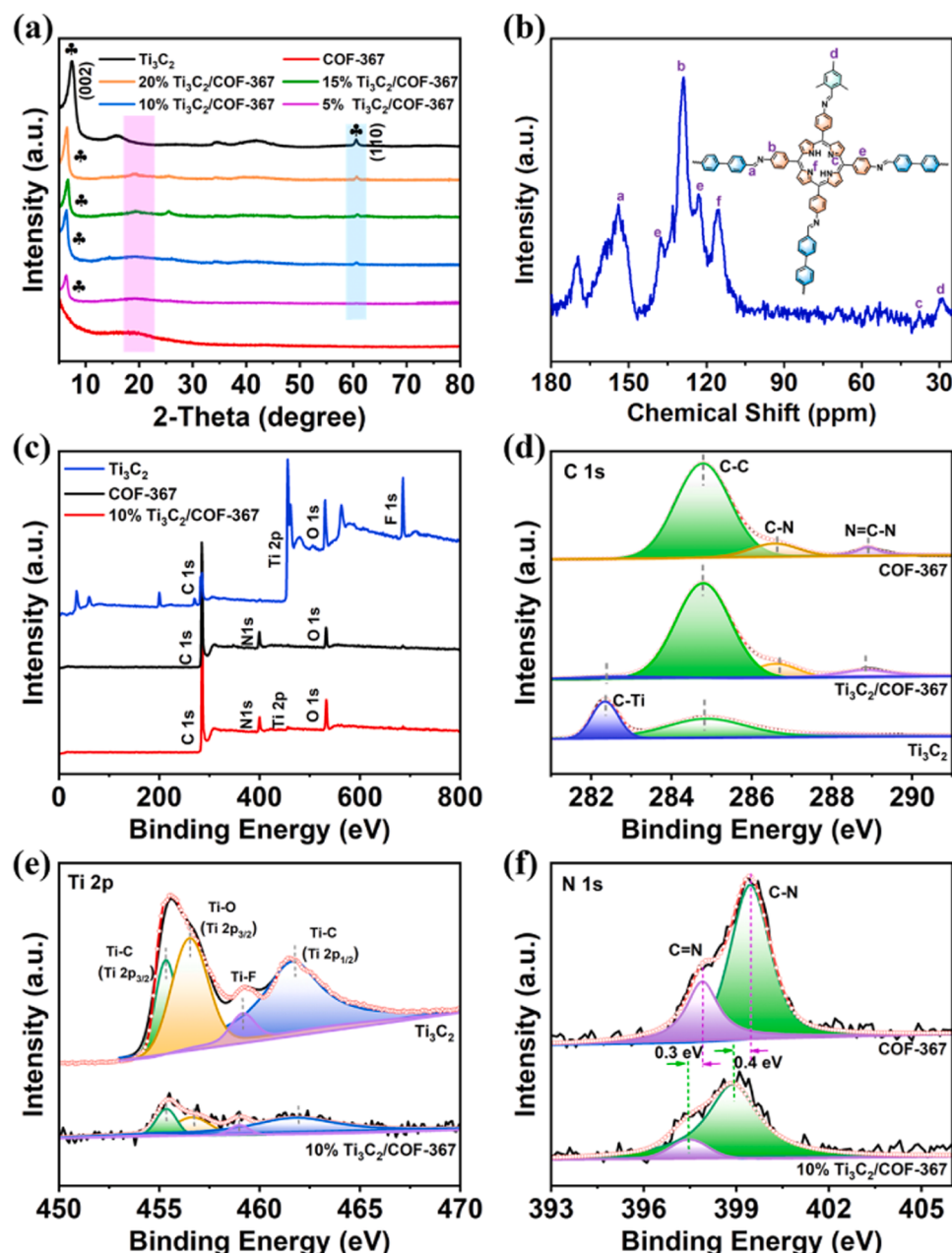


Fig. 3. (a) XRD patterns, (b) solid-state ^{13}C NMR of COF-367, and (c) XPS spectra of as-prepared samples. High resolution XPS spectra of (d) C 1s, (e) Ti 2p, and (f) N 1s.

planes [39]. On the other hand, the ultrathin COF-367 only exhibited a broad peak around 20° , which is reasonable considering its few stacked layers (Fig. S5a). As expected, all $\text{Ti}_3\text{C}_2/\text{COF-367}$ hybrids displayed characteristic XRD peaks of both Ti_3C_2 and COF-367 without observation of any impurities. The intensities of these peaks increased and decreased, respectively, with the increasing content of MXene, further indicating the successful combination of well-designed 2D/2D heterostructures (Fig. S5b). Solid-state ^{13}C NMR spectrum of COF-367 indicates the successful construction of its molecular structure (Fig. 3b). The carbon peaks at 156, 126, 38, and 29 ppm are attributed to the C=N, benzene ring skeleton, C-N, -CH₃, respectively [27,34]. Moreover, the carbon signals of olefin (C=C) carbon (120 and 137 ppm) and cyano groups (115 ppm) also prove the synthesis of COF-367 [40,41]. However, the peaks at 133 ppm and 169 ppm derive from carbonyl and amide [41,42], possibly causing by the excessive TBA. The MS of H₂TAPP and MALDI-MS of COF-367 were detected to prove the precursor purity of COF-367. As shown in Fig. S6-7, all of the characteristic peaks can be attributed to ionic fragments ionized by the COF-367 material without other impurities, thus illustrating the relative purity of COF-367 [43]. Subsequently, FT-IR spectra were recorded to verify

the successful synthesis of samples by examining the vibration of chemical bonds. As illustrated in Fig. S8, COF-367 exhibits several vibrational peaks corresponding to specific chemical bonds, while Ti_3C_2 does not show distinct stretching vibration signals, possibly due to its rigid structure [44]. The FT-IR signals observed in $\text{Ti}_3\text{C}_2/\text{COF-367}$ hybrids mainly originate from COF-367. The peaks at 1622 and 800 cm^{-1} can be attributed to C=N stretching vibrations and the out-of-plane bending vibration of C-H, respectively. The bands observed at 2800–3100 and 3200–3400 cm^{-1} are associated with the stretching vibrations of =C-H and N-H groups, respectively [45].

XPS was used to analyze the chemical compositions and surface chemical states of the prepared photocatalysts. The spectra of Ti_3C_2 , COF-367 and 10 % $\text{Ti}_3\text{C}_2/\text{COF-367}$ confirm the presence of all respective elements without other elements, illustrating the purity of samples (Fig. 3c). It is important to note that the presence of O and F elements in MXene can be attributed to the etching process [46], while the weak peak of Ti in the heterojunction is due to the low Ti_3C_2 content. Specifically, the binding energies of 284.8, 286.6, and 288.8 eV correspond to C-C, C-N, and N=C-N bonds in COF-367, respectively (Fig. 3d). In contrast, Ti_3C_2 exhibits peaks at 282.3, 284.8, and 287.9 eV,

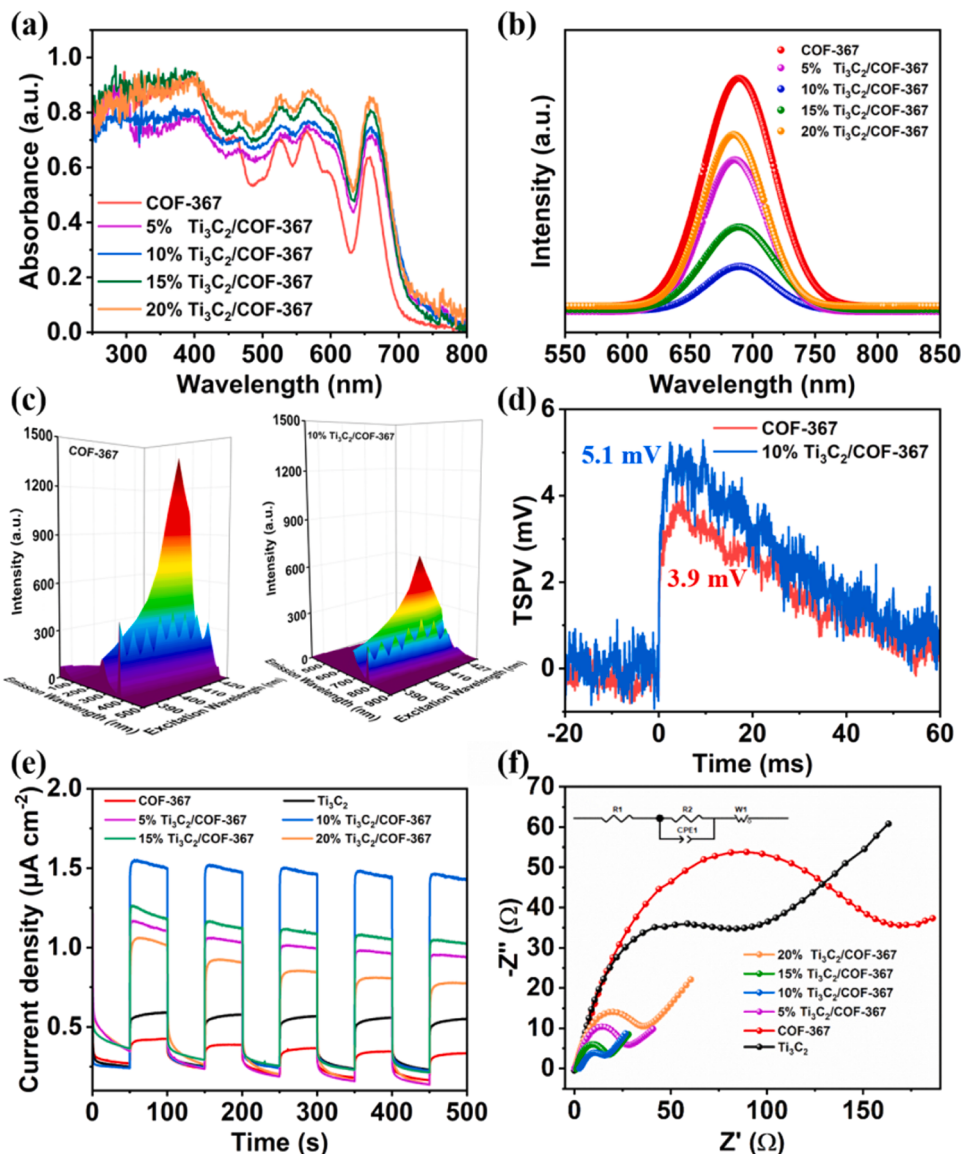


Fig. 4. (a) UV-Vis DRS, (b) PL spectra, (c) fluorescence emission-excitation 3D maps, (d) TSPV spectra, (e) photocurrent transient response, and (f) EIS plots of the as-prepared samples.

corresponding to Ti-C, C-C and C-F bonds, respectively [47]. The reduced intensity of the Ti-C bond peak in 10 % $\text{Ti}_3\text{C}_2/\text{COF-367}$ can be associated with the lower MXene content. In the Ti 2p region, four peaks at 455.4, 456.5, 459.2, and 461.6 eV represent Ti-C ($\text{Ti} 2\text{p}_{3/2}$), Ti-O, Ti-F and Ti-C ($\text{Ti} 2\text{p}_{1/2}$), respectively [28,48] (Fig. 3e). The O 1s spectra are analyzed in Fig. S9 [49]. The N 1s spectra show peaks at 397.9 and 399.4 eV belong to C=N and C-N bonds in COF-367. These peaks exhibit a shift towards lower binding energies of approximately 0.3–0.4 eV following the formation of $\text{Ti}_3\text{C}_2/\text{COF-367}$ (Fig. 3f), suggesting an intense interaction between MXene and COF-367 in the heterojunction [50]. The intense interaction also increases availability of electrons for MXene in the heterojunction.

3.3. Optical and spatial charge separation properties

UV-Vis DRS demonstrate the remarkable light absorption properties of COF-367, particularly in the visible region (Fig. 4a). Simultaneously,

Ti_3C_2 presents strong light absorption capacity from 250 nm to 800 nm with no obvious absorption edge, implying its metallic character without bandgap (Fig. S10a). Pristine COF-367 exhibits a broad absorption edge at approximately 710 nm, corresponding to a band energy of 1.74 eV, as determined by the Tauc plots: $(ah\nu)^2 = A(h\nu - E_g)$ [51] (Fig. S10b). Notably, the visible-light absorption range of COF-367 surpasses that of currently reported photocatalytic materials [43]. As expected, the visible light absorption intensity of $\text{Ti}_3\text{C}_2/\text{COF-367}$ hybrid is further enhanced with an increase in Ti_3C_2 content, with an absorption edge at about 750 nm, laying a strong foundation for its potential exceptional photocatalytic capability.

The spatial charge separation abilities of the samples were investigated using various techniques, including steady-state PL, TSPV, transient photocurrent responses, and EIS plots. As illustrated in Fig. 4b, all samples exhibit an emission peak around 690 nm when excited by a 410 nm laser. In contrast, the PL peak intensity of 10 % $\text{Ti}_3\text{C}_2/\text{COF-367}$ is the lowest, indicating reduced radiative recombination of

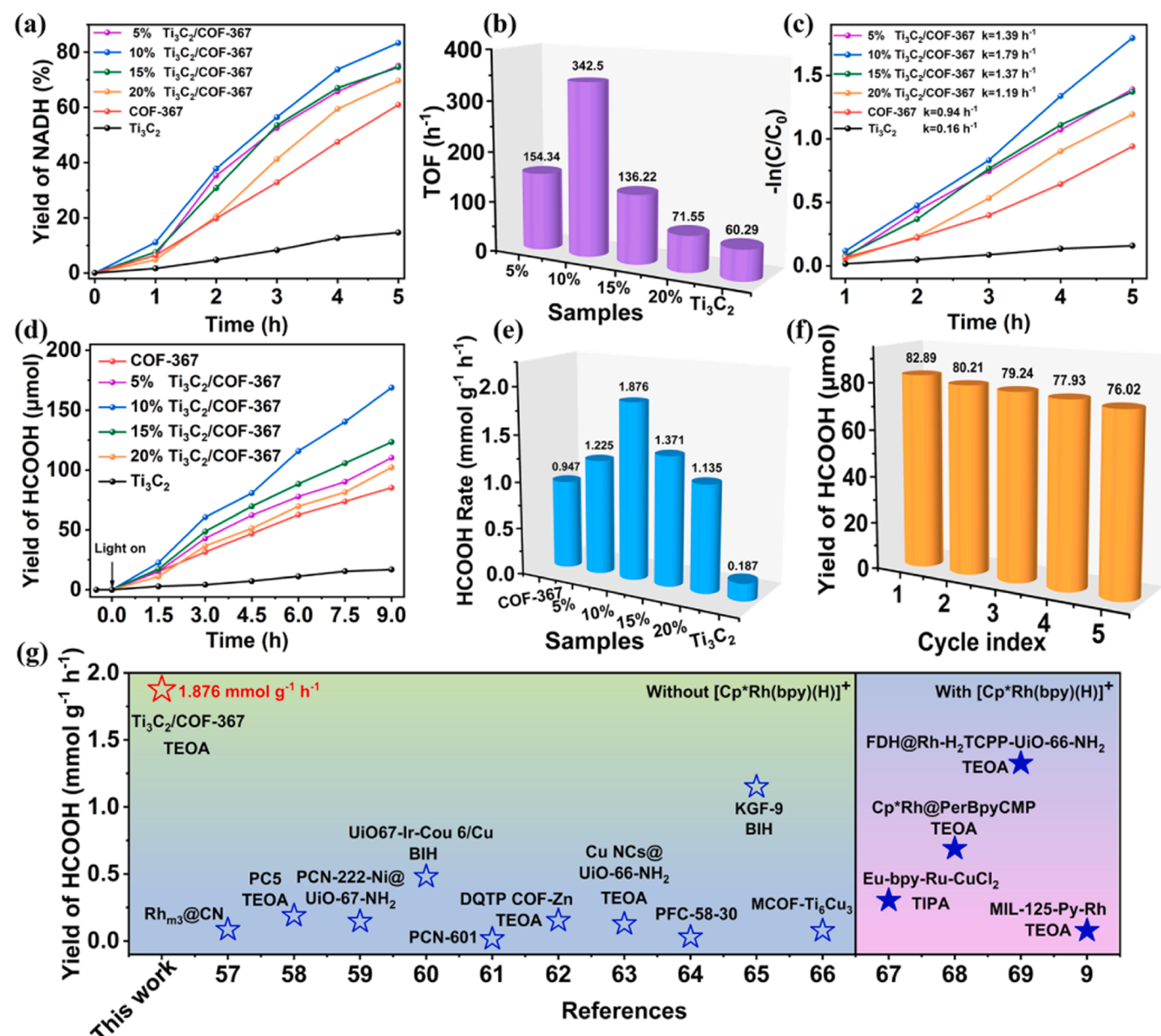


Fig. 5. (a) Photocatalytic NADH regeneration performance, corresponding (b) TOF and (c) kinetics analysis, (d) HCOOH yields of the samples and (e) corresponding generation rates. (f) HCOOH production performance of 10 % $\text{Ti}_3\text{C}_2/\text{COF-367}$ in a multi-cycle production process (4 hours per cycle). (g) Comparison of HCOOH yield of 10 % $\text{Ti}_3\text{C}_2/\text{COF-367}$ with those reported in the literatures [9,57–69].

photogenerated carriers. This observation is further supported by the fluorescence emission-excitation 3D maps of COF-367 and 10 % $\text{Ti}_3\text{C}_2/\text{COF-367}$ under different excitation wavelengths (Fig. 4c). The TSPV spectra intuitively demonstrate the separation and decay of photogenerated charge carriers in the samples. As depicted in Fig. 4d, 10 % $\text{Ti}_3\text{C}_2/\text{COF-367}$ exhibits a higher transient photovoltage of 5.1 mV compared to COF-367 (3.9 mV), implying its rapid separation of photogenerated carriers. Additionally, it demonstrates a slower decay, suggesting its potential for higher photocatalytic activity [52]. This conclusion is further confirmed by the transient photocurrent-time with 50 s light on/off cycles (Fig. 4e). At the moment of turning on/off the light source, the photocurrent density of the samples rapidly increases/decreases and quickly stabilizes, indicating their sensitivity to solar light. Furthermore, the smallest EIS Nyquist arc radius of 10% $\text{Ti}_3\text{C}_2/\text{COF-367}$ implies its smallest charge transfer resistance (Fig. 4f) [53]. These results collectively demonstrate that the incorporation of Ti_3C_2 effectively enhances the separation and transfer of photogenerated carriers in COF-367, while also inhibiting recombination and slowing down charge decay.

3.4. Photocatalytic performance

The photocatalytic performance of the samples was evaluated by NADH regeneration without $[\text{Cp}^*\text{Rh}(\text{bpy})\text{H}_2\text{O}]^{2+}$ electron mediator or photosensitizer, and further through the photoenzymatic synergistic cascade catalysis of CO_2 conversion to HCOOH with the assistant of FDH. As shown in Fig. S11a, the peak intensity (265 nm) of $\beta\text{-NAD}^+$ gradually decrease and finally stabilize during 0.5 h dark treatment, illustrating $\beta\text{-NAD}^+$ adsorption achieve equilibrated. It is calculated that the adsorption of $\beta\text{-NAD}^+$ stabilized at about nearly 20% in dark treatment (Fig. S11b). Afterwards, the NADH regeneration on different samples are detected. As illustrated in Fig. 5a, 10 % $\text{Ti}_3\text{C}_2/\text{COF-367}$ exhibits the highest NADH yield of 83.38 % after 5 hours of irradiation. This yield is 1.32 and 5.48 times higher than that of pristine COF-367 (60.97 %) and Ti_3C_2 (14.68 %), respectively. Moreover, it surpasses the reported values in most literature even with the use of $[\text{Cp}^*\text{Rh}(\text{bpy})(\text{H})]^+$ electron mediator (Fig. S12). Based on the estimated BET surface area of Ti as the active site, the corresponding turnover frequency (TOF) of 10 % $\text{Ti}_3\text{C}_2/\text{COF-367}$ is calculated to be 342.5 h^{-1} according to the formula: $\text{TOF} = \frac{\text{Amounts of product molecules}}{\text{moles of active site} \times \text{Reaction time}(\text{h})}$ (Fig. 5b) [12,54]. The photocatalytic NADH regeneration kinetics were further analyzed by plotting the natural logarithm of the generated NADH concentration against the reaction time (Fig. 5c), which indicates that the photocatalytic reaction follows first-order kinetics. The kinetic constant (k) was determined using the equation $\ln(C_0/C_t) = kt$ [55], and it was found that 10 % $\text{Ti}_3\text{C}_2/\text{COF-367}$ behaves the highest k value of 1.79 h^{-1} . These results collectively demonstrate that MXene is an effective assistant in enhancing the photocatalytic performance of COF-367.

The *in situ* generated NADH can undergo further photoenzymatic synergistic cascade catalysis to convert CO_2 to HCOOH with the assistance of FDH. In this photoenzyme-catalyzed system, HCOOH can be continuously produced with the infinite circulation of $\beta\text{-NAD}^+$ and NADH. As anticipated, after 9 hours of irradiation, the highest HCOOH yield of 168.8 μmol was achieved with 10 % $\text{Ti}_3\text{C}_2/\text{COF-367}$, and the HCOOH selectivity was nearly 100 %, without other carbon-containing byproducts (Fig. 5d). This yield is 2.0 times higher than that of COF-367 (85.3 μmol) and 10.0 times higher than that of Ti_3C_2 (16.9 μmol). The corresponding HCOOH production rates are displayed in Fig. 5e, indicating that a Ti_3C_2 content of 10 % is the optimum value for $\text{Ti}_3\text{C}_2/\text{COF-367}$ hybrids. Based on previous photoelectric performance test results, it can be speculated that the effective enhancement of separation and transport of photogenerated carriers in COF-367 may be attributed to the incorporation of MXene. This, in turn, enhances the photocatalytic performance of COF-367. Therefore, $\text{Ti}_3\text{C}_2/\text{COF-367}$ heterojunction exhibits a significantly higher HCOOH yield ($1.88 \text{ mmol g}^{-1} \text{ h}^{-1}$) even

without Rh-based electron mediator, surpassing the reported cases (Fig. 5g). Moreover, the photocatalytic ability of bulk COF-367 and COF-367 nanosheets are invested in Fig. S13. Whether NADH regeneration or CO_2 conversion, COF-367 nanosheets shows better photocatalytic performance than bulk COF-367. The ultrathin structure of COF-367 nanosheets also enhance the photocatalytic ability due to more surface reaction sites and suitable band structure [56]. In addition, the good stability of the prepared 2D/2D $\text{Ti}_3\text{C}_2/\text{COF-367}$ heterojunction was demonstrated by its stable HCOOH yield (4 hours per cycle) after 5-cycle experiments (Fig. 5f). The slight decrease observed may be attributed to experimental errors and FDH consumption. The morphology, crystallinity, chemical structure and optical properties of 10 % $\text{Ti}_3\text{C}_2/\text{COF-367}$ were maintained after cycling experiments according to TEM, XRD, FT-IR and PL spectra (Fig. S14-16), further suggesting its stability. The controlled experiments are carried out to verify the role of FDH and NADH. As shown in Fig. S17, the main products of photocatalytic CO_2 reduction on 10 % $\text{Ti}_3\text{C}_2/\text{COF-367}$ is CO and CH_4 . After 5 h illumination, the lower yield of CO ($0.012 \text{ mmol g}^{-1} \text{ h}^{-1}$) and CH_4 ($0.015 \text{ mmol g}^{-1} \text{ h}^{-1}$) with lower selectivity (71 % of CO and 29 % of CH_4) compared with photoenzymatic HCOOH yield ($1.880 \text{ mmol g}^{-1} \text{ h}^{-1}$ with nearly 100 % selectivity), stressing the importance of FDH and NADH.

3.5. Photocatalytic mechanism

To investigate the photocatalytic mechanism of the 2D/2D $\text{Ti}_3\text{C}_2/\text{COF-367}$ heterostructure for efficient NADH regeneration and the photoenzymatic synergistic cascade catalysis of CO_2 conversion to HCOOH, the energy band structure of COF-367 was initially explored. UV-Vis DRS results revealed a band energy of 1.74 eV for COF-367. Through M-S plots, its flat band was determined to be -1.64 V (vs Ag/AgCl, pH = 7). Moreover, the positive slope in M-S plots confirmed its *n*-type semiconductor characteristics (Fig. 6a). As a result, its conduction band (CB) level can be approximated to the flat band owing to its *n*-type nature, [70] while the valance band (VB) value was calculated to be 0.30 V (vs NHE, pH = 7) using the formulate: $\text{E}_{\text{VB}} = \text{E}_{\text{CB}} + \text{E}_g$. Importantly, the CB potential of COF-367 is more negative than the redox potential of NAD^+/NADH (-0.32 V vs NHE, pH = 7) [71], indicating its suitability for the thermodynamic conversion of NAD^+ into NADH, and favorable for the subsequent conversion of CO_2 into HCOOH.

To gain a better understanding of the electronic structure of COF-367, we conducted first-principles DFT calculations using VASP and PBE method for the exchange-correlation potential. A tetragonal crystal structure of COF-367 model was used, with a periodic porphyrin imine structure selected as the crystalline cell structure model (Fig. 6b and Fig. S18). The fractional atomic coordinates for the crystal structure model of COF-367 with an eclipsed arrangement was displayed in Table S2. As illustrated in Fig. 6c, COF-367 exhibits a metal-free property, as both the spin-up and spin-down bands do not across Fermi level. It indicates that COF-367 has a narrow bandgap of 0.71 eV , which is smaller than the value calculated by experimental method. This difference can be attributed to the characterization of PBE method [72-74]. It is worth noting that the total density of states (DOS) of COF-367 is mainly contributed by C element. The presence of horizontal lines in the electronic band gap structure may be attributed to the doping of N element, which facilitates the transport and enrichment of photogenerated electrons.

Based on the aforementioned experimental results and theoretical DFT calculations, we propose a plausible photocatalytic mechanism for $\text{Ti}_3\text{C}_2/\text{COF-367}$ heterostructure in NADH regeneration and photoenzymatic synergistic cascade catalysis of CO_2 to HCOOH (Fig. 6d). Upon exposure to sunlight, the photogenerated e^- and h^+ in COF-367 undergo charge separation. Electrons are excited to the CB, while h^+ remain in the VB. The excellent conductivity of Ti_3C_2 nanosheets facilitates the rapid enrichment of e^- on its surface through interfacial electron transfer, effectively preventing charge recombination. The enriched e^- on Ti_3C_2 nanosheets then participate in the reduction of NAD^+ to

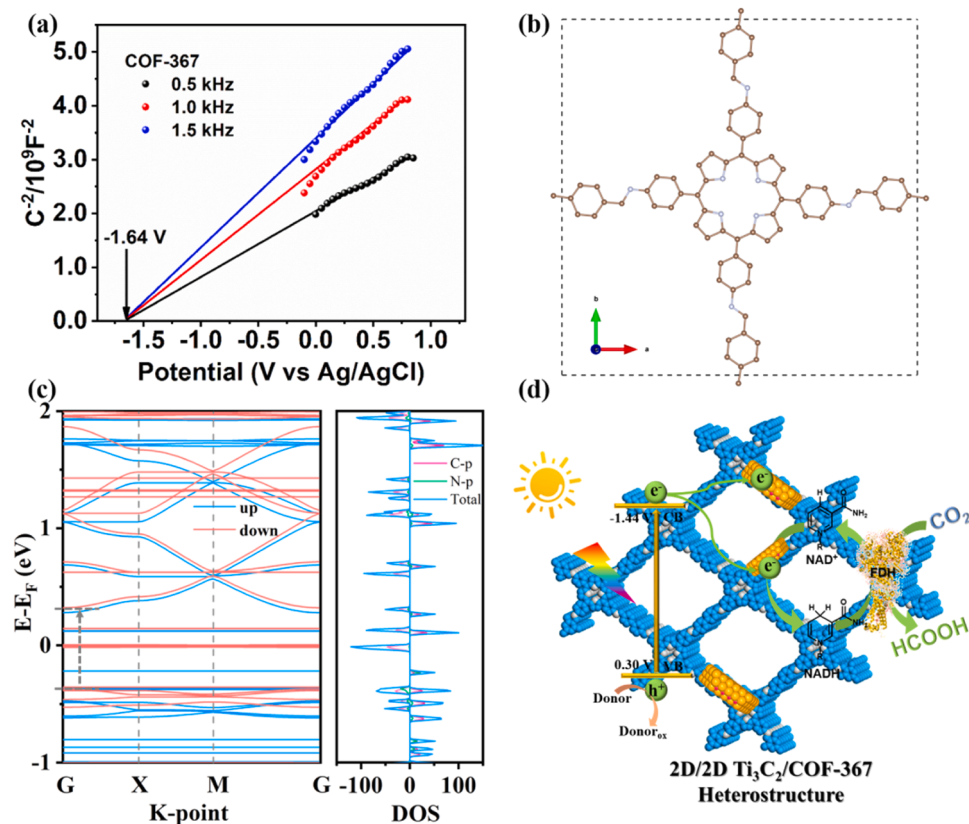


Fig. 6. (a) M-S plots, (b) calculated electronic band structure and (c) DOS of COF-367. (d) The proposed photocatalytic mechanism of $Ti_3C_2/COF-367$ heterostructure under visible light irradiation.

coenzyme NADH, assisting the bioenzyme FDH in the targeted conversion of CO_2 to HCOOH. Simultaneously, NADH is oxidized back to NAD^+ , completing a $NAD^+/NADH$ cycle that promotes the sustainable conversion of CO_2 to HCOOH [75]. This photocatalytic mechanism takes advantage of efficient charge separation and interfacial electron transfer in the $Ti_3C_2/COF-367$ heterostructure. Fig. 6d illustrates the key steps involved in this photocatalytic process, highlighting the charge separation, electron enrichment on Ti_3C_2 , and the $NAD^+/NADH$ cycle. Through this mechanism, the 2D/2D $Ti_3C_2/COF-367$ heterostructure holds great promise for sustainable and efficient NADH regeneration and the conversion of CO_2 to HCOOH.

4. Conclusion

In summary, we have successfully developed an efficient artificial photosynthesis platform using a 2D/2D Ti_3C_2 /crystalline COF-367 heterostructure for excellent NADH regeneration and photoenzymatic synergistic cascade catalysis in the conversion of CO_2 to HCOOH. The highly crystalline imine-linked COF-367 was synthesized through a solvothermal nucleophilic addition reaction, and its morphology was precisely regulated into 2D ultrathin nanosheets by grafting rigid TBA molecules at the edges. The well-designed 2D/2D Ti_3C_2 /crystalline COF-367 heterostructure with abundant hetero-interfaces exhibited excellent responsiveness to visible light ($\lambda \leq 750$ nm), facilitating rapid charge separation and transfer performance. Consequently, it achieved an impressive NADH regeneration yield of 83.38 % without electron mediator, coupled with an ultra-high HCOOH production rate of $1.88 \text{ mmol g}^{-1} \text{ h}^{-1}$ with an almost 100 % selectivity. This research not only designs a novel artificial photosynthesis platform by constructing an organic/inorganic heterojunction interface but also offers effective strategies for the highly selective conversion of CO_2 into value-added chemicals.

CRediT authorship contribution statement

Jundie Hu: Writing – review & editing, Supervision, Project administration, Funding acquisition, Conceptualization. **Chang Ming Li:** Writing – review & editing, Supervision. **Xiaogang Yang:** Visualization, Validation. **Yahui Cai:** Investigation. **Fengyi Yang:** Software, Formal analysis. **Pengye Zhang:** Methodology, Investigation. **Tingyu Yang:** Writing – original draft, Investigation, Data curation. **Jiafu Qu:** Writing – original draft, Methodology, Investigation, Funding acquisition.

Declaration of Competing Interest

The authors declare that they have no known competing financial interests or personal relationships that could have appeared to influence the work reported in this paper.

Data availability

Data will be made available on request.

Acknowledgements

The authors gratefully acknowledge the financial support provided by National Natural Science Foundation of China (22008163), Natural Science Foundation of Jiangsu Province (BK20231342, BK20210867), Open Project Program of the State Key Laboratory of Photocatalysis on Energy and Environment (SKLPEE-KF202309), Natural Science Research Project of Higher Education Institutions in Jiangsu Province (21KJB150038).

Appendix A. Supporting information

Supplementary data associated with this article can be found in the online version at doi:10.1016/j.apcatb.2024.123827.

References

- [1] M. Bonchio, J. Bonin, O. Ishitani, T.-B. Lu, T. Morikawa, A.J. Morris, E. Reisner, D. Sarkar, F.M. Toma, M. Robert, Best practices for experiments and reporting in photocatalytic CO_2 reduction, *Nat. Catal.* 6 (2023) 657–665.
- [2] E. Gong, S. Ali, C.B. Hiragond, H.S. Kim, N.S. Powar, D. Kim, H. Kim, S.-I. In, Solar fuels: Research and development strategies to accelerate photocatalytic CO_2 conversion into hydrocarbon fuels, *Energy Environ. Sci.* 15 (2022) 880–937.
- [3] C. Ning, J. Yang, S. Bai, G. Chen, G. Liu, T. Shen, L. Zheng, S.-M. Xu, X. Kong, B. Liu, Y. Zhao, Y.-F. Song, An efficient intercalation supramolecular structure for photocatalytic CO_2 reduction to ethylene under visible light, *Adv. Funct. Mater.* 33 (2023) 2300365.
- [4] K. Kosugi, C. Akatsuka, H. Iwami, M. Kondo, S. Masaoka, Iron-complex-based supramolecular framework catalyst for visible-light-driven CO_2 Reduct., *J. Am. Chem. Soc.* 145 (2023) 10451–10457.
- [5] S. Cheng, Z. Sun, K.H. Lim, T.Z.H. Gani, T. Zhang, Y. Wang, H. Yin, K. Liu, H. Guo, T. Du, L. Liu, G.K. Li, Z. Yin, S. Kawi, Emerging strategies for CO_2 photoreduction to CH_4 : from experimental to data-driven design, *Adv. Energy Mater.* 12 (2022) 2200389.
- [6] D. Li, K. Yang, J. Lian, J. Yan, S. Liu, Powering the world with solar fuels from photoelectrochemical CO_2 reduction: basic principles and recent advances, *Adv. Energy Mater.* 12 (2022) 2201070.
- [7] Z. Zhao, D. Zheng, M. Guo, J. Yu, S. Zhang, Z. Zhang, Y. Chen, Engineering olefin-linked covalent organic frameworks for photoenzymatic reduction of CO_2 , *Angew. Chem. Int. Ed.* 61 (2022) e202200261.
- [8] A. Zhang, X. Zhuang, J. Liu, J. Huang, L. Lin, Y. Tang, S. Zhao, R. Li, B. Wang, B. Fang, W. Hong, Catalytic cycle of formate dehydrogenase captured by single-molecule conductance, *Nat. Catal.* 6 (2023) 266–275.
- [9] G. Lin, Y. Zhang, Y. Hua, C. Zhang, C. Jia, D. Ju, C. Yu, P. Li, J. Liu, Bioinspired metalation of the metal-organic framework MIL-125-NH₂ for photocatalytic NADH regeneration and gas-liquid-solid three-phase enzymatic CO_2 reduction, *Angew. Chem. Int. Ed.* 61 (2022) e202206283.
- [10] J.A. Bau, A.-H. Emwas, P. Nikolaienko, A.A. Aljarb, V. Tung, M. Rueping, Mo^{3+} hydride as the common origin of H_2 evolution and selective NADH regeneration in molybdenum sulfide electrocatalysts, *Nat. Catal.* 5 (2022) 397–404.
- [11] K.P. Sokol, W.E. Robinson, A.R. Oliveira, J. Warnan, M.M. Nowaczyk, A. Ruff, I.A. C. Pereira, E. Reisner, Photoreduction of CO_2 with a formate dehydrogenase driven by photosystem II using a semi-artificial Z-Scheme, *Archit.*, *J. Am. Chem. Soc.* 140 (2018) 16418–16422.
- [12] Y. Sun, J. Shi, Z. Wang, H. Wang, S. Zhang, Y. Wu, H. Wang, S. Li, Z. Jiang, Thylakoid membrane-inspired capsules with fortified cofactor shuttling for enzyme-photocoupled catalysis, *J. Am. Chem. Soc.* 144 (2022) 4168–4177.
- [13] J. Liu, X. Ren, C. Li, M. Wang, H. Li, Q. Yang, Assembly of COFs layer and electron mediator on silica for visible light driven photocatalytic NADH regeneration, *Appl. Catal. B* 310 (2022) 121314.
- [14] Y. Li, W. Chen, G. Xing, D. Jiang, L. Chen, New synthetic strategies toward covalent organic frameworks, *Chem. Soc. Rev.* 49 (2020) 2852–2868.
- [15] T. He, Y. Zhao, Covalent organic frameworks for energy conversion in photocatalysis, *Angew. Chem. Int. Ed.* 62 (2023) e202303086.
- [16] Y. Luo, B. Zhang, C. Liu, D. Xia, X. Ou, Y. Cai, Y. Zhou, J. Jiang, B. Han, Sulfone-modified covalent organic frameworks enabling efficient photocatalytic hydrogen peroxide generation via one-step two-electron O_2 reduction, *Angew. Chem. Int. Ed.* 62 (2023) e202305355.
- [17] Y. Wang, H. Liu, Q. Pan, C. Wu, W. Hao, J. Xu, R. Chen, J. Liu, Z. Li, Y. Zhao, Construction of fully conjugated covalent organic frameworks via facile linkage conversion for efficient photoenzymatic catalysis, *J. Am. Chem. Soc.* 142 (2020) 5958–5963.
- [18] W. Dong, Z. Qin, K. Wang, Y. Xiao, X. Liu, S. Ren, L. Li, Isomeric oligo(phenylenevinylene)-based covalent organic frameworks with different orientation of imine bonds and distinct photocatalytic activities, *Angew. Chem. Int. Ed.* 62 (2023) e202216073.
- [19] J. Jing, J. Li, Y. Su, Y. Zhu, Non-covalently linked donor-acceptor interaction enhancing photocatalytic hydrogen evolution from porphyrin assembly, *Appl. Catal. B* 324 (2023) 122284.
- [20] J. Jing, J. Yang, W. Li, Z. Wu, Y. Zhu, Construction of interfacial electric field via dual-porphyrin heterostructure boosting photocatalytic hydrogen evolution, *Adv. Mater.* 34 (2022) 2106807.
- [21] Z. Chen, J. Wang, M. Hao, Y. Xie, X. Liu, H. Yang, G.I.N. Waterhouse, X. Wang, S. Ma, Tuning excited state electronic structure and charge transport in covalent organic frameworks for enhanced photocatalytic performance, *Nat. Commun.* 14 (2023) 1106.
- [22] L. Yang, H. Li, Y. Yu, Y. Wu, L. Zhang, Assembled 3D MOF on 2D nanosheets for self-boosting catalytic synthesis of N-doped carbon nanotube encapsulated metallic Co electrocatalysts for overall water splitting, *Appl. Catal. B* 271 (2020) 118939.
- [23] L. Yang, G. Sun, H. Fu, L. Zhang, Isolation of cobalt single atoms on hollow B, N Co-doped defective carbon nanotubes for hydrogen peroxide production and tandem reagent-free electro-Fenton oxidation, *Chem. Eng. J.* 472 (2023) 145052.
- [24] Y. Wei, P. Zhang, R.A. Soomro, Q. Zhu, B. Xu, Advances in the synthesis of 2D MXenes, *Adv. Mater.* 33 (2021) 2103148.
- [25] L. Xiao, L. Qi, J. Sun, A. Husile, S. Zhang, Z. Wang, J. Guan, Structural regulation of covalent organic frameworks for advanced electrocatalysis, *Nano Energy* 120 (2024) 109155.
- [26] Y. Wang, W. Hao, H. Liu, R. Chen, Q. Pan, Z. Li, Y. Zhao, Facile construction of fully sp^2 -carbon conjugated two-dimensional covalent organic frameworks containing benzobisthiazole units, *Nat. Commun.* 13 (2022) 100.
- [27] W. Liu, X. Li, C. Wang, H. Pan, W. Liu, K. Wang, Q. Zeng, R. Wang, J. Jiang, A scalable general synthetic approach toward ultrathin imine-linked two-dimensional covalent organic framework nanosheets for photocatalytic CO_2 reduction, *J. Am. Chem. Soc.* 141 (2019) 17431–17440.
- [28] C. Lu, A. Li, G. Li, Y. Yan, M. Zhang, Q. Yang, W. Zhou, L. Guo, S-decorated porous Ti_3C_2 MXene combined with in situ forming Cu_2Se as effective shuttling interrupter in *nas* batteries, *Adv. Mater.* 33 (2021) 2008414.
- [29] H. Wang, C. Qian, J. Liu, Y. Zeng, D. Wang, W. Zhou, L. Gu, H. Wu, G. Liu, Y. Zhao, Integrating suitable linkage of covalent organic frameworks into covalently bridged inorganic/organic hybrids toward efficient photocatalysis, *J. Am. Chem. Soc.* 142 (2020) 4862–4871.
- [30] J. Shi, S. Fan, X. Li, P. Wang, Y. Mao, M. Wang, G. Chen, Artificial thylakoid membrane assisted $\text{NiMn}_2\text{O}_4@\text{PoPDA}$ hierarchical hollow nanospheres for photo-enzyme integrated catalysis, *Appl. Catal. B* 342 (2024) 123434.
- [31] G. Kresse, D. Joubert, From ultrasoft pseudopotentials to the projector augmented-wave method, *Phys. Rev. B* 59 (1999) 1758–1775.
- [32] J.P. Perdew, K. Burke, M. Ernzerhof, Generalized gradient approximation made simple, *Phys. Rev. Lett.* 77 (1996) 3865–3868.
- [33] W. Liu, X. Li, C. Wang, H. Pan, W. Liu, K. Wang, Q. Zeng, R. Wang, J. Jiang, A scalable general synthetic approach toward ultrathin imine-linked two-dimensional covalent organic framework nanosheets for photocatalytic CO_2 Reduct., *J. Am. Chem. Soc.* 141 (2019) 17431–17440.
- [34] Y.-N. Gong, W. Zhong, Y. Li, Y. Qiu, L. Zheng, J. Jiang, H.-L. Jiang, Regulating photocatalysis by spin-state manipulation of cobalt in covalent organic frameworks, *J. Am. Chem. Soc.* 142 (2020) 16723–16731.
- [35] J. Tan, S. Namuengruk, W. Kong, N. Kungwan, J. Guo, C. Wang, Manipulation of amorphous-to-crystalline transformation: Towards the construction of covalent organic framework hybrid microspheres with NIR photothermal conversion ability, *Angew. Chem. Int. Ed.* 55 (2016) 13979–13984.
- [36] Y. Wu, W. Xu, L. Jiao, W. Gu, D. Du, L. Hu, Y. Lin, C. Zhu, Nanobiocatalysis: A materials science road to biocatalysis, *Chem. Soc. Rev.* 51 (2022) 6948–6964.
- [37] Q. Chen, Y. Wang, G. Luo, Photoenzymatic CO_2 reduction dominated by collaborative matching of linkage and linker in covalent organic frameworks, *J. Am. Chem. Soc.* 146 (2024) 586–598.
- [38] X. Li, J. Hu, T. Yang, X. Yang, J. Qu, C.M. Li, Efficient photocatalytic H_2 -evolution coupled with valuable furfural-production on exquisite 2D/2D $\text{LaVO}_4/\text{g-C}_3\text{N}_4$ heterostructure, *Nano Energy* 92 (2022) 106714.
- [39] D. Zhao, P. Wang, H. Di, P. Zhang, X. Hui, L. Yin, Single semi-metallic selenium atoms on Ti_3C_2 MXene nanosheets as excellent cathode for lithium-oxygen batteries, *Adv. Funct. Mater.* 31 (2021) 2010544.
- [40] S. Bi, P. Thiruvengadam, S. Wei, W. Zhang, F. Zhang, L. Gao, J. Xu, D. Wu, J.-S. Chen, F. Zhang, Vinylene-bridged two-dimensional covalent organic frameworks via knoevenagel condensation of tricyanomesitylene, *J. Am. Chem. Soc.* 142 (2020) 11893–11900.
- [41] Z. Wang, Y. Zhang, E. Lin, S. Geng, M. Wang, J. Liu, Y. Chen, P. Cheng, Z. Zhang, Kilogram-scale fabrication of a robust olefin-linked covalent organic framework for separating ethylene from a ternary C_2 hydrocarbon mixture, *J. Am. Chem. Soc.* 145 (2023) 21483–21490.
- [42] Z.-B. Zhou, X.-H. Han, Q.-Y. Qi, S.-X. Gan, D.-L. Ma, X. Zhao, A facile, efficient, and general synthetic method to amide-linked covalent organic frameworks, *J. Am. Chem. Soc.* 144 (2022) 1138–1143.
- [43] K. Wang, Y. Zhong, W. Dong, Y. Xiao, S. Ren, L. Li, Intermediate formation of macrocycles for efficient crystallization of 2D covalent organic frameworks with enhanced photocatalytic hydrogen evolution, *Angew. Chem. Int. Ed.* 62 (2023) e202304611.
- [44] Y. Yang, Z. Zeng, G. Zeng, D. Huang, R. Xiao, C. Zhang, C. Zhou, W. Xiong, W. Wang, M. Cheng, W. Xue, H. Guo, X. Tang, D. He, Ti_3C_2 mxene/porous $\text{g-C}_3\text{N}_4$ interfacial schottky junction for boosting spatial charge separation in photocatalytic H_2O_2 production, *Appl. Catal. B* 258 (2019) 117956.
- [45] F. He, B. Zhu, B. Cheng, J. Yu, W. Ho, W. Macyk, 2D/2D/0D $\text{TiO}_2/\text{C}_3\text{N}_4/\text{Ti}_3\text{C}_2$ MXene composite S-scheme photocatalyst with enhanced CO_2 reduction activity, *Appl. Catal. B* 272 (2020) 119006.
- [46] Q. Xue, H. Zhang, M. Zhu, Z. Pei, H. Li, Z. Wang, Y. Huang, Y. Huang, Q. Deng, J. Zhou, S. Du, Q. Huang, C. Zhi, Photoluminescent Ti_3C_2 MXene quantum dots for multicolor cellular imaging, *Adv. Mater.* 29 (2017) 1604847.
- [47] X. Han, L. An, Y. Hu, Y. Li, C. Hou, H. Wang, Q. Zhang, Ti_3C_2 MXene-derived carbon-doped TiO_2 coupled with $\text{g-C}_3\text{N}_4$ as the visible-light photocatalysts for photocatalytic H_2 generation, *Appl. Catal. B* 265 (2020) 118539.
- [48] C. Yang, Q. Tan, Q. Li, J. Zhou, J. Fan, B. Li, J. Sun, K. Lv, 2D/2D Ti_3C_2 MXene/ $\text{g-C}_3\text{N}_4$ nanosheets heterojunction for high efficient CO_2 reduction photocatalyst: dual effects of urea, *Appl. Catal. B* 268 (2020) 118738.
- [49] J. Xia, S.-Z. Yang, B. Wang, P. Wu, I. Popovs, H. Li, S. Irle, S. Dai, H. Zhu, Boosting electrosynthesis of ammonia on surface-engineered MXene Ti_3C_2 , *Nano Energy* 72 (2020) 104681.
- [50] J. Zheng, X. Liu, L. Zhang, Design of porous double-shell $\text{Cu}_2\text{O}@\text{CuCo}_2\text{O}_4$ Z-Scheme hollow microspheres with superior redox property for synergistic photocatalytic degradation of multi-pollutants, *Chem. Eng. J.* 389 (2020) 124339.
- [51] J. Fang, H. Fan, M. Li, C. Long, Nitrogen self-doped graphitic carbon nitride as efficient visible light photocatalyst for hydrogen evolution, *J. Mater. Chem. A* 3 (2015) 13819–13826.

[52] H. Zeng, Z. Li, G. Li, X. Cui, M. Jin, T. Xie, L. Liu, M. Jiang, X. Zhong, Y. Zhang, H. Zhang, K. Ba, Z. Yan, Y. Wang, S. Song, K. Huang, S. Feng, Interfacial engineering of $\text{TiO}_2/\text{Ti}_3\text{C}_2$ MXene/carbon nitride hybrids boosting charge transfer for efficient photocatalytic hydrogen evolution, *Adv. Energy Mater.* 12 (2022) 2102765.

[53] X.-L. Pu, X.-C. Yang, S.-S. Liang, W. Wang, J.-T. Zhao, Z.-J. Zhang, Self-assembly of a $\text{g-C}_3\text{N}_4$ -based 3D aerogel induced by N-modified carbon dots for enhanced photocatalytic hydrogen production, *J. Mater. Chem. A* 9 (2021) 22373–22379.

[54] Y. Kuramochi, Y. Fujisawa, A. Satake, Photocatalytic CO_2 reduction mediated by electron transfer via the excited triplet state of Zn(II) porphyrin, *J. Am. Chem. Soc.* 142 (2020) 705–709.

[55] F. Dalanta, T.D. Kusworo, Synergistic adsorption and photocatalytic properties of AC/ $\text{TiO}_2/\text{CeO}_2$ composite for phenol and ammonia-nitrogen compound degradations from petroleum refinery wastewater, *Chem. Eng. J.* 434 (2022) 134687.

[56] X. Sun, H. Huang, Q. Zhao, T. Ma, L. Wang, Thin-layered photocatalysts, *Adv. Funct. Mater.* 30 (2020) 1910005.

[57] Y. Zhang, X. Kan, Y. Zou, J. Liu, Non-covalent metalation of carbon nitride for photocatalytic NADH regeneration and enzymatic CO_2 reduction, *Chem. Commun.* 58 (2022) 10997–11000.

[58] P. Wang, X. Ba, X. Zhang, H. Gao, M. Han, Z. Zhao, X. Chen, L. Wang, X. Diao, G. Wang, Direct Z-scheme heterojunction of PCN-222/CsPbBr₃ for boosting photocatalytic CO_2 reduction to HCOOH, *Chem. Eng. J.* 457 (2023) 141248.

[59] H.-B. Huang, Z.-B. Fang, R. Wang, L. Li, M. Khanpour, T.-F. Liu, R. Cao, Engineering hierarchical architecture of metal-organic frameworks for highly efficient overall CO_2 photoreduction, *Small* 18 (2022) 2200407.

[60] S. Guo, L.-H. Kong, P. Wang, S. Yao, T.-B. Lu, Z.-M. Zhang, Switching excited state distribution of metal-organic framework for dramatically boosting photocatalysis, *Angew. Chem. Int. Ed.* 61 (2022) e202206193.

[61] Q. Huang, R. Wang, X. Li, T. Liu, A.R.M. Shaheer, R. Cao, The effects of local environment towards yield and selectivity on photocatalytic CO_2 reduction catalyzed by metal-organic framework, *Chin. Chem. Lett.* 34 (2023) 108517.

[62] M. Lu, Q. Li, J. Liu, F.-M. Zhang, L. Zhang, J.-L. Wang, Z.-H. Kang, Y.-Q. Lan, Installing earth-abundant metal active centers to covalent organic frameworks for efficient heterogeneous photocatalytic CO_2 reduction, *Appl. Catal. B* 254 (2019) 624–633.

[63] S. Dai, T. Kajiwara, M. Ikeda, I. Romero-Muñiz, G. Patriarche, A.E. Platero-Prats, A. Vimont, M. Daturi, A. Tissot, Q. Xu, C. Serre, Ultrasmall copper nanoclusters in zirconium metal-organic frameworks for the photoreduction of CO_2 , *Angew. Chem. Int. Ed.* 61 (2022) e202211848.

[64] A.-A. Zhang, D. Si, H. Huang, L. Xie, Z.-B. Fang, T.-F. Liu, R. Cao, Partial metalation of porphyrin moieties in hydrogen-bonded organic frameworks provides enhanced CO_2 photoreduction activity, *Angew. Chem. Int. Ed.* 61 (2022) e202203955.

[65] Y. Kamakura, S. Yasuda, N. Hosokawa, S. Nishioka, S. Hongo, T. Yokoi, D. Tanaka, K. Maeda, Selective CO_2 -to-formate conversion driven by visible light over a precious-metal-free nonporous coordination polymer, *ACS Catal.* 12 (2022) 10172–10178.

[66] J. Zhou, J. Li, L. Kan, L. Zhang, Q. Huang, Y. Yan, Y. Chen, J. Liu, S.-L. Li, Y.-Q. Lan, Linking oxidative and reductive clusters to prepare crystalline porous catalysts for photocatalytic CO_2 reduction with H_2O , *Nat. Commun.* 13 (2022) 4681.

[67] T.-C. Zhuo, Y. Song, G.-L. Zhuang, L.-P. Chang, S. Yao, W. Zhang, Y. Wang, P. Wang, W. Lin, T.-B. Lu, Z.-M. Zhang, H-bond-mediated selectivity control of formate versus CO during CO_2 photoreduction with two cooperative Cu/X sites, *J. Am. Chem. Soc.* 143 (2021) 6114–6122.

[68] F.M. Wisser, M. Duguet, Q. Perrinet, A.C. Ghosh, M. Alves-Favarro, Y. Mohr, C. Lorentz, E.A. Quadrelli, R. Palkovits, D. Farrusseng, C. Mellot-Draznieks, V. de Waele, J. Canivet, Molecular porous photosystems tailored for long-term photocatalytic CO_2 reduction, *Angew. Chem. Int. Ed.* 59 (2020) 5116–5122.

[69] X. Xing, Y. Liu, R.-D. Lin, Y. Zhang, Z.-L. Wu, X.-Q. Yu, K. Li, N. Wang, Development of an integrated system for highly selective photoenzymatic synthesis of formic acid from CO_2 , *ChemSusChem* 16 (2023) e202201956.

[70] K. Xiong, Y. Wang, F. Zhang, X. Li, X. Lang, Linker length-dependent photocatalytic activity of β -ketoenamine covalent organic frameworks, *Appl. Catal. B* 322 (2023) 122135.

[71] S. Li, Y. Cheng, Y. Chen, J. Li, Y. Sun, J. Shi, Z. Jiang, Topologically and chemically engineered conjugated polymer with synergistically intensified electron generation, transfer and utilization for photocatalytic nicotinamide cofactor regeneration, *Appl. Catal. B* 317 (2022) 121772.

[72] Y. Wang, F. Silveri, M.K. Bayazit, Q. Ruan, Y. Li, J. Xie, C.R.A. Catlow, J. Tang, Bandgap engineering of organic semiconductors for highly efficient photocatalytic water splitting, *Adv. Energy Mater.* 8 (2018) 1801084.

[73] J. Li, A. Slassi, X. Han, D. Cornil, M.-H. Ha-Thi, T. Pino, D.P. Debecker, C. Colbeau-Justin, J. Arbiol, J. Cornil, M.N. Ghazzal, Tuning the electronic bandgap of graphdiyne by H-substitution to promote interfacial charge carrier separation for enhanced photocatalytic hydrogen production, *Adv. Funct. Mater.* 31 (2021) 2100994.

[74] S. Wang, K. Ge, H. Cui, S. Li, Y. Yang, M. Pan, L. Zhu, Self-polarization-enhanced oxygen evolution reaction by flower-like core-shell $\text{BaTiO}_3/\text{NiFe}$ -layered double hydroxide heterojunctions, *Chem. Eng. J.* 479 (2024) 147831.

[75] X. Wang, T. Saba, H.H.P. Yiu, R.F. Howe, J.A. Anderson, J. Shi, Cofactor NAD(P)H regeneration inspired by heterogeneous pathways, *Chem* 2 (2017) 621–654.